energies

MDPI

Article

Enhancement of Renewable Power System Protection Reliability Using a Superconducting Fault Current Limiting Circuit Breaker (SFCL-CB)

Sangjae Choi [1,2] and Sung-Hun Lim [2,*]

[1] Korea Electrical Safety Corporation, 111, Anjeon-ro, Iseo-myeon, Wanju-gun 55365, Jeonbuk-state, Republic of Korea; choisj203@kesco.or.kr
[2] Department of Electrical Engineering, Soongsil University, 369 Sangdo-ro, Dongjak-gu, Seoul 06978, Republic of Korea
* Correspondence: superlsh73@ssu.ac.kr; Tel.: +82-2-828-7268

Abstract

The proliferation of inverter-based resources (IBRs) and energy storage systems in power grids has led to a decline in the short-circuit ratio (SCR) and reduced fault current magnitudes, compromising the reliability of conventional overcurrent relays (OCRs) and creating protection blind zones. To resolve these vulnerabilities, this paper proposes an electromagnetic repulsion-based Superconducting Fault Current-Limiting Circuit Breaker (SFCL-CB) utilizing a flux-lock type mechanism. Unlike protection schemes that rely on secondary accessories such as current and potential transformers which introduce computational delays, the proposed SFCL-CB utilizes a driving force that scales with the square of the current gradient ($(di/dt)^2$). This characteristic allows the device to distinguish low-magnitude fault currents from transient load growths. Through duality-based modeling and parametric simulations in PSCAD/EMTDC, the structural and electrical design configurations—including the coil turns (N_1, N_2) and the superconducting quench resistance (R_{SC})—were optimized. The simulation results verify that the proposed SFCL-CB substantially reduces the OCR blind zone, securing fault clearance within a maximum of 0.131 s in the regions cleared under low SCR and high-fault-resistance conditions, while achieving mechanical separation in 0.0048 s under robust power system. This SFCL-CB offers an alternative to enhance the protection reliability and operational stability of distribution power system.

Keywords: superconducting fault current limiter; circuit breaker; protection blind zone; inverter-based resources; short-circuit ratio; di/dt-based fault detection

Check for updates

Academic Editor: Stéphane Grieu

Received: 26 June 2026
Revised: 26 July 2026
Accepted: 18 August 2026
Published: 20 August 2026

Copyright: © 2026 by the authors. Licensee MDPI, Basel, Switzerland. This article is an open access article distributed under the terms and conditions of the Creative Commons Attribution (CC BY) license.

1. Introduction

The rapid proliferation of solar energy resources and Energy Storage Systems (ESS) significantly increases power system impedance and decreases the Short-Circuit Ratio (SCR) [1,2]. Since inverter-based resources (IBRs) lack the physical rotating inertia of conventional generators, they provide limited fault current, leading to a reduction in short-circuit capacity [3,4]. Consequently, when a fault occurs, the fault current does not flow at a high magnitude, yet voltage fluctuations become significant. This system environment leads to frequent misoperation of overcurrent relays (OCRs) responsible for fault detection (in the sense of protection misoperation, covering both failure to trip and false trip as defined in IEEE Std C37.100) [5]. While damage from overcurrent may be

reduced, electrical equipment remains vulnerable to failures caused by undervoltage, and the fault itself may go undetected due to the relay's failure to operate.

Therefore, in IBR-dominant grids, it is crucial to maintain high sensitivity to fault currents while clearly distinguishing them from transient load increases to prevent both false trip (undesired operation during non-fault conditions such as load growth) and failure to trip (missed detection during actual fault conditions). Even in IBR-dominant systems, it is necessary to consider the inverse-time characteristics of OCRs, where the tripping speed accelerates according to the magnitude of the fault current, like conventional power systems. Generally, the sensitivity of the OCR is determined by the pickup current, I_{pickup}. Setting a low I_{pickup} allows for tripping at smaller current levels; however, this causes the relay to react sensitively not only to fault currents but also to current rises from increased loads, leading to risks of failure to trip or false trip.

To address these issues, research has focused on adjusting OCR settings by incorporating voltage or directional elements [6–9]. However, these methods require additional accessories such as Current Transformers (CT), Potential Transformers (PT), and computational units, which complicates the protection system and extends the trip time. This paper proposes a Superconducting Fault Current-Limiting Circuit Breaker (SFCL-CB) capable of enhancing sensitivity to fault currents while simultaneously distinguishing them from current rises caused by load increases. This is complemented by recent work on directional overcurrent relay coordination for systems with inverter-based resources [10–12].

Existing protection families addressing IBR-dominated systems either rely on high-bandwidth communication and time synchronization (differential protection, double-ended travelling-wave location), require online parameter estimation or training data (adaptive and intelligent relaying), or lose sensitivity under low fault current levels (conventional overcurrent relays, including negative-sequence variants). No lightweight, device-level protection mechanism has yet been reported that discriminates faults from load growth using an intrinsic electromagnetic response, without external CT/PT or communication accessories. This is the gap that the present research addresses.

Table 1 summarizes representative protection techniques reported in recent reviews of IBR-influenced protection [13–17], contrasting travelling-wave-based protection, differential protection, directional overcurrent protection, and adaptive or intelligent relaying with the proposed SFCL-CB. Values explicitly reported in the cited references are listed.

Table 1. Comparison of Protection Techniques for Low-SCR, IBR-Dominated Systems, using the characterizations reported in the cited reviews [13–17].

Method	Fault Detection Principle	Sensitivity/Blind-Zone Behavior Under IBR/Low SCR	Communication and Requirements	Complexity
Travelling-wave-based protection [13,14]	Detection of high-frequency transient wavefronts launched by the fault	Less affected by inverter control since the method operates below the IBR control response window [13]	High-sampling-rate transducers, precise time-stamping/GPS synchronization; higher hardware cost [14]	High computational requirement noted in [13]
Differential protection [12]	Phasor-based comparison of currents measured at both line ends	Sensitivity, starting-logic, and phase-selection issues on the IBR side due to low fault current magnitude and altered phase-angle characteristics [13]	Communication channel and time synchronization between both terminals; CTs at both ends	Requires adaptation for IBR-connected lines [13]
Directional overcurrent [12]	Directional element combined with overcurrent pickup	Pickup may fail because the negative-sequence current supplied by IBRs is often below the activation threshold; direction determination affected by altered voltage/current angle relationship [13]	CT and PT for polarization; time-graded coordination	Time-graded inverse or definite characteristic

Table 1. *Cont.*

Method	Fault Detection Principle	Sensitivity/Blind-Zone Behavior Under IBR/Low SCR	Communication and Requirements	Complexity
Adaptive or intelligent relaying [12,15]	Online adjustment of relay settings based on system state, optionally combined with ML/optimization	Improved via adaptive settings and communication-based coordination; effectiveness bounded by communication reliability and data availability [16]	IED plus central controller (MPMC); communication (typically IEC 61850 [17], target latency ~4 ms); optionally ML or optimization algorithm requiring training data [13]	Additional processing delay at the IED
Proposed SFCL-CB	Intrinsic electromagnetic mechanism with driving force proportional to $(di/dt)^2$	OCR blind zone substantially reduced over the SCR and R_fault ranges tested, with a residual region at SCR = 1 combined with high fault resistance	No CT/PT or communication; superconducting element and cryogenic cooling required	Low computational requirement (no digital processing)

Table 1 shows that several of the schemes reviewed in [13–17] depend either on high-bandwidth communication (differential protection, double-ended travelling-wave location) or on online parameter estimation combined with communication (adaptive and intelligent relaying), which introduce latency and infrastructure requirements documented in the cited references. In terms of operating principle, the SFCL-CB achieves fault discrimination through an intrinsic electromagnetic mechanism proportional to $(di/dt)^2$, without external CT/PT or communication accessories.

To cancel self-inductance, non-inductive winding methods such as Bifilar Winding or Ayrton-Perry Winding are commonly employed. Structurally, these methods eliminate inductance by allowing opposing currents to flow through two windings in a manner that cancels the magnetic flux, thereby preventing self-induction. This approach offers the advantage of reducing both steady-state impedance and transient inductance to zero.

In contrast, the proposed Superconducting Fault Current-Limiting Circuit Breaker (SFCL-CB) is based on the flux-lock type fault current limiter, which achieves magnetic balance by winding two coils onto a single iron core and connecting a superconducting element in parallel to one of the windings [18–23]. This structure leverages the zero-impedance characteristic of the superconducting element under normal conditions to maintain magnetic balance. This balanced state ensures that no voltage is induced across windings N_1 and N_2 during normal operation, providing zero total impedance to the SFCL-CB. However, during transient states where the current rises, the magnetic balance is disrupted due to the differing physical time constants of N_1 and N_2 circuits. Consequently, magnetic flux is no longer cancelled within the core but becomes linked [23].

Distinguishing between fault currents and current increases due to load growth in systems with a low Short-Circuit Ratio (SCR) remains a significant challenge in modern power system protection research. Although methods utilizing voltage elements, directional elements, and current rise rates (di/dt) exist, they are economically inefficient as they require various accessories such as PTs and CTs. Furthermore, the computational delays inherent in these processes cause another issue by reducing the breaking speed.

While fault detection methods using the current rise, rate exploit the fact that fault currents increase very rapidly, they typically require a process involving a CT, a differentiator, and a comparator to evaluate the magnitude. This series of steps inevitably delays the tripping time. Notably, the current rise rate, di/dt, can be indirectly determined through the voltage across the inductance. Since Bifilar or Ayrton-Perry Winding methods physically maintain zero inductance, they face the limitation of being unable to measure the voltage resulting from fault currents.

However, during a fault, the differing physical time constants of N_1 and N_2 cause a millisecond-scale delay in magnetic balance, creating a transient imbalance that induces a voltage across N_1. This induced voltage directly drives a Thomson coil, generating an initial repulsive force ($\boldsymbol{F}$) through electromagnetic reaction with the eddy currents in the Moving Plate (MP). Because both the magnetic field and the eddy current intensity are proportional to the primary current's rate of change, the resulting force $\boldsymbol{F}$ is proportional to $(di/dt)^2$.

$$F \propto \left(\frac{di}{dt}\right)^2 \tag{1}$$

By Faraday's law, the transient imbalance voltage induced across N_1 is $v_1 = d\lambda/dt$, which is proportional to di/dt. This voltage drives the Thomson coil current, whose associated magnetic flux density B is likewise proportional to di/dt. The eddy current induced in the moving plate is governed by the same current derivative, $i_{\text{eddy}} \propto dB/dt \propto di/dt$. Since the electromagnetic repulsion force is proportional to the product of the flux density and the eddy current, $F \propto B \cdot i_{\text{eddy}}$, combining these proportionalities yields $F \propto (di/dt)^2$, as expressed in Equation (1). Equations (2)–(4) follow the standard mutual-inductance formulation, and Equations (14)–(19) are based on the reluctance formulation given by Joseph [24].

This mechanism allows the SFCL-CB to distinguish fault-driven surges from gradual load increases without secondary accessories, ensuring rapid and selective protection. This study evaluates the electrical and physical characteristics of the proposed system through PSCAD/EMTDC (Power System Computer Aided Design/Electromagnetic Transients DC) electromagnetic-physical simulations.

2. Materials and Methods

The proposed model integrates a circuit breaker (CB) with a superconducting fault current limiter (SFCL) and is recognized for resolving the coordination issues that arise from the inherent operation of the SFCL. Generally, an SFCL is installed upstream of the CB to reduce the magnitude of fault currents. However, if the current is limited below the CB's trip threshold, a secondary accident may occur where the CB fails to trip, resulting in a protection failure (failure to trip). To address this, the SFCL-CB was devised as an integrated unit. The SFCL-CB is designed to actuate the breaker's trip coil by monitoring the resistance, voltage, and current variations occurring within the superconducting element, thereby ensuring reliable fault isolation even during current limiting conditions.

2.1. Flux-Lock Type SFCL

A flux-lock type Superconducting Fault Current Limiter (SFCL) consists of two or more coils coupled through a magnetic circuit, with a superconducting element electrically connected to the secondary coil. The magnetic field generated by the primary coil influences the secondary coil via the magnetic circuit, inducing back electromotive force (EMF). This induced EMF drives a current through the secondary circuit, which in turn generates a magnetic field in a direction that opposes the change in the original flux. Consequently, the intensity of this opposing magnetic field is determined by the secondary current. If the secondary circuit has zero resistance, the secondary coil produces a magnetic field that completely cancels the flux from the primary coil. This state, where the magnetic flux is suppressed or "locked," is referred to as the "flux-lock" state.

To achieve this, the flux-lock type SFCL connects a superconducting element in series with the secondary coil, ensuring that the secondary circuit resistance remains near zero under normal conditions. When the primary and secondary fluxes are perfectly cancelled, the effective inductance of the coils becomes zero, resulting in a total steady-state

impedance near zero. However, once the secondary current exceeds the critical current (*Ic*) of the superconductor, the element transitions to a resistive state (quench). In this state, the secondary coil can no longer fully cancel the primary magnetic fluxes, temporarily "unlocking" the magnetic circuit. This leads to the generation of inductance throughout the circuit, providing the SFCL with the necessary impedance to limit the fault current.

The flux-lock type SFCL allows for the adjustment of the secondary current magnitude by varying the turns ratio (tap ratio) between the coils, thereby enabling indirect control of the superconducting element's critical current. This capability allows for the fine-tuning of the SFCL's sensitivity. Furthermore, since the full fault current does not flow directly through the superconducting element, this configuration is advantageous for protecting the element from excessive thermal and electrical stress.

The superconducting element considered in this study is a $YBa_2Cu_3O_{-x}$ (YBCO) coated conductor operating at 77 K in a liquid-nitrogen cryostat, consistent with the flux-lock type SFCL trial units reported in [18–23], and within the range of HTS SFCL material properties studied in [25]. The quench-resistance range used in the parametric sweep (R_{SC} = 0.8–10 Ω) falls within the operating range of this material.

2.2. SFCL-CB

The flux-lock type SFCL-CB refers to a circuit breaker that leverages these specific characteristics. It operates on the same principle of maintaining a magnetic balance by utilizing two or more coils and at least one superconducting (SC) element. However, in this configuration, the primary (N_1) and secondary (N_2) coils function as the driving coils of the circuit breaker. When a quench occurs in the SC element, a magnetic field is generated, exerting an electromagnetic force on the breaker's moving plate (MP). This enables the simultaneous execution of fault current limiting and interruption within a single device.

Figure 1 illustrates the structure of the flux-lock type SFCL-CB. Under normal operating conditions, the SC element maintains zero resistance, allowing current to flow exclusively through the SC path rather than N_2. Since the voltage across the SC element is zero, the voltage across the parallel-connected N_2 also remains at zero. With no electromotive force (EMF) induced in N_2, the induced EMF in N_1 likewise stays at zero. Consequently, the magnetic fields generated by N_1 and N_2 cancel each other out, achieving a state of magnetic balance, which results in a total impedance of zero. However, once resistance develops in the SC element, the magnetic fields between N_1 and N_2 no longer cancel. In this state, the inductances generated by N_1 and N_2 are defined as follows:

$$v_1 = L_1 \frac{di_{N1}(t)}{dt} + M \frac{di_{N2}(t)}{dt} \tag{2}$$

$$v_2 = L_2 \frac{di_{N2}(t)}{dt} + M \frac{di_{N1}(t)}{dt} \tag{3}$$

Assuming a turns ratio of N_1:N_2 = *a*:*b*,

$$L_1 = \frac{\mu S N_1^2}{l},\ L_2 = \frac{\mu S N_2^2}{l},\ M = \frac{\mu S k^2 N_1 N_2}{l} \tag{4}$$

In this context, k represents the coupling coefficient; assuming an ideal magnetic coupling, k is equal to 1. In a practical core, flux leakage between the N_1 and N_2 windings causes k to be slightly less than 1, which reduces the imbalance voltage induced across N_1 during a fault and results in a marginally lower driving force and a correspondingly longer clearing time. The term M denotes the mutual inductance between N_1 and N_2, with its sign determined by the dot convention. The dot orientation shown in Figure 1 indicates subtractive polarity, where v_{N1} and v_{N2} share the same positive sign. Conversely, if the dot on N_2 is reversed, v_{N2} takes a negative sign according to the dot convention, resulting in

additive polarity. Consequently, the direction of the current flowing to cancel the magnetic flux is also reversed.

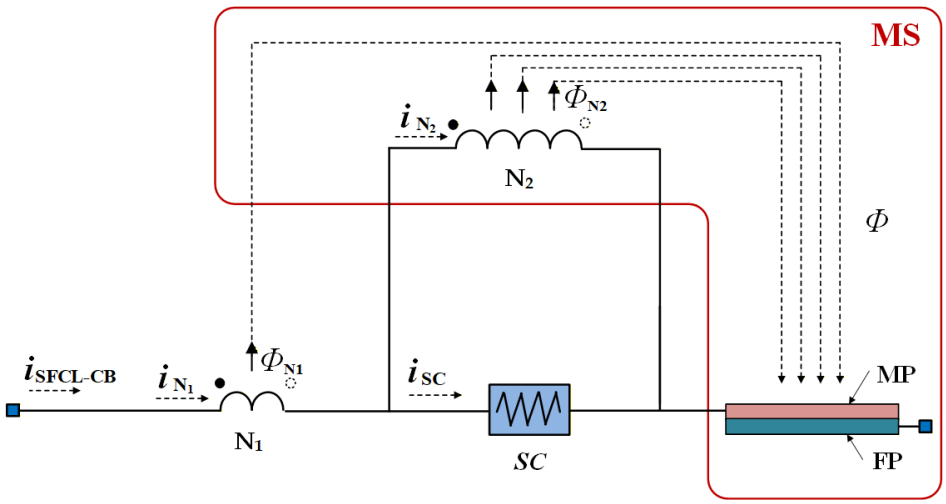


Figure 1. Electromagnetic Equivalent Circuit of the proposed SFCL-CB (Superconducting Fault Current Limiting-circuit Breaker).

Specifically, based on Kirchhoff's Current Law (KCL), the relationship is defined as $i_{N1} = i_{N2} + i_{SC}$ for subtractive polarity, and $i_{N1} + i_{N2} = i_{SC}$ for additive polarity. Assuming i_{N1} remains constant, the magnitude of i_{SC} varies depending on the polarity. Therefore, additive polarity is suitable for increasing the sensitivity of the superconducting (SC) element, while subtractive polarity is more appropriate for protecting the SC element and reducing its sensitivity.

The intensity of the magnetic field induced in the moving plate (MP) is directly related to the resistance of the SC element. As the resistance increases, the magnetic balance between N_1 and N_2 is further disrupted, leading to a stronger induced magnetic field in the MP. Accordingly, the magnetic field intensity is greater in the additive polarity configuration—where higher currents flow—resulting in a stronger electromagnetic force for opening the circuit breaker.

When designing the proposed SFCL-CB, the primary considerations are to ensure that the moving plate (MP) receives sufficient repulsive force within a short duration and that circuit interruption is completed within 2 ms. To allow for adequate current flow, the inductances of N_1 and N_2 must be kept low. The MP should be lightweight yet thicker than the skin depth, and strong magnetic coupling must be established between the coils and the MP. Structurally, the N_1 and N_2 coils wrap around an I-shaped core, with the MP integrated into the core in the form of the annular ring. A mechanical block is positioned at the top of the I-core to prevent the MP from moving beyond the height of the core. By co-winding or layering N_1 and N_2, the magnetic coupling is enhanced, and the MP is placed immediately above the coils to maximize the initial coupling strength.

A maximum voltage of 22.9 kV can be applied across N_1 and N_2. Accordingly, the volts-per-turn (e_t) and the length of the core must be carefully determined. In typical 22.9 kV transformers, a voltage of 20–30 V/turn is used, resulting in approximately 1100 turns. However, such a high number of turns would lead to excessive inductance and winding resistance, which might overly limit the fault current and fail to generate the repulsive force necessary for MP movement.

In eddy current magnetic levitation, while the repulsive force can be derived from both the Lorentz force and magnetic energy (W_m), the influence of magnetic energy is generally more dominant. The enthalpy of the isolated system always acts in a direction

that minimizes energy. Although the fault current significantly increases the magnetic energy, the system tends to lower this energy, exerting a force in a direction that increases magnetic reluctance. The following equation defines the magnetic energy:

$$W_m = \frac{1}{2}\mathcal{F} \cdot \phi \tag{5}$$

Substituting the relation for magnetic reluctance into Equation (5),

$$\phi = \frac{\mathcal{F}}{\mathcal{R}} = \frac{N \cdot I}{\mathcal{R}} \tag{6}$$

$$W_m = \frac{1}{2}\frac{\mathcal{F}^2}{\mathcal{R}} = \frac{1}{2}\phi^2 \cdot \mathcal{R} = \frac{1}{2}\phi^2 \cdot (\mathcal{R}_{core} + \mathcal{R}_{leak}) \tag{7}$$

The energy supplied from the power system is distributed into the variation of magnetic energy and the mechanical work, defined as $\int f(x) \cdot dx$. In a state where there is no external energy supply—or at a momentary duration where the magnetic flux remains constant—the mechanical work performed as the plate moves by an infinitesimal distance dx is equivalent to the variation in magnetic energy.

$$F \cdot dx = |dW_m| \tag{8}$$

$$F = \frac{\partial W_m}{\partial x} \tag{9}$$

Since the moving plate proposed in this study does not exceed the maximum height of the iron core, it can be assumed that the magnitude of the magnetic flux remains constant regardless of the displacement. Consequently, the variation in energy relative to the change in magnetic reluctance ($\mathcal{R}$) can be differentiated as follows:

$$F = \frac{\partial W_m}{\partial x} = \frac{\mathrm{d}}{\mathrm{dx}}\left(\frac{1}{2}\phi^2 \cdot \mathcal{R}(x)\right) \tag{10}$$

As previously assumed, the magnetic flux can be treated as a constant. Furthermore, considering that the force is generated in a direction that minimizes magnetic reluctance, it is assigned a negative ($-$) sign.

$$F_{repulsion} = -\frac{1}{2}\phi^2 \frac{\mathrm{d}\mathcal{R}(x)}{\mathrm{dx}} \tag{11}$$

The equation of motion for the mechanical displacement of the moving plate is determined by two primary forces: the magnetic repulsive force and gravity. While air resistance and frictional resistance at the contact surface between the core and the moving plate may occur during movement, these can be neglected under specific assumptions. Specifically, air resistance is negligible if the contacts are placed in a vacuum, and frictional resistance can be ignored by assuming that both the core and the moving plate are homogeneous and isotropic. Based on these assumptions, the equation of motion can be derived as follows:

$$m\frac{d^2x}{dt^2} = F_{total} = F_{repulsion}(\phi,\ x, \mathcal{R}) - F_{gravity} \tag{12}$$

Neglecting air resistance and mechanical friction in Equation (12) leads to a slight underestimation of the mechanical delay of the moving plate. Under the vacuum-sealed contact and homogeneous-material assumptions considered in this study, this contribution constitutes a second-order correction relative to the dominant electromagnetic repulsion force. These three effects are examined in Section 2.3.

The position x of the moving plate can be obtained by integrating the equation of motion and is given by

$$x = \frac{1}{m}\left\{\iint_{t_0}^{t} F_{total} \cdot d\tau + V_0 t + x_0\right\} (where,\ v_0 = 0,\ x_0 = 0.001\ \text{mm}) \tag{13}$$

According to Equation (11), the total force (F_{total}) is dependent on the magnetic reluctance, which in turn varies with the displacement (x) of the moving plate. Consequently, accurate modeling of the magnetic reluctance is essential for the precise simulation of the moving plate's dynamics. The magnetic circuit can be broadly categorized into the internal and external of the iron core. The internal magnetic reluctance is determined by the length, cross-sectional area, and relative permeability of the core.

$$\mathcal{R}_{core} = \frac{l_{core}}{\mu A_{core}} \tag{14}$$

The external magnetic circuit is further subdivided into air-path return reluctance and leakage reluctance. The air-path return reluctance represents the path where the magnetic flux spreads from the top of the I-core in a hemispherical shape (fringing effect) and reconverges at the bottom of the core. Generally, since the magnetic field propagates hemispherically from a point source and varies according to the distance, it can be mathematically formulated using integration.

$$\mathcal{R}_{top} = \int_{r_1}^{r_2} \frac{dr}{\mu_0(2\pi r^2)} = \frac{1}{2\pi\mu_0}\left(\frac{1}{r_1} - \frac{1}{r_2}\right) = \frac{1}{2\pi\mu_0 \cdot \sqrt{A}} \tag{15}$$

In this model, r_1 can be considered the effective radius of the iron core, defined as $r_1 = \sqrt{A}$. While r_2 is typically assumed to be half the length of the core, this study treats it as an infinite value. Since the magnetic flux spreading from the top of the core returns through the side surfaces in a cylindrical pattern, it can be defined as follows:

$$R_{body} = \frac{L}{\mu_0 \cdot A_{eff}} \tag{16}$$

Here, A_{eff} represents an approximated space for the extensive air path, which varies according to the aspect ratio between the core length L and the radius r_1 [22]. Joseph characterized the demagnetizing factors N_a, N_b and N_c based on the aspect ratio p (=L/r_1); an increase in p results in a smaller N_a, which implies a larger effective cross-sectional area and lower magnetic reluctance. For the structure proposed in this paper, since p is 5.06 (≈0.2 m/0.0395 m), A_{eff} is assumed to be 54A (cross-section), following the relation $A_{eff} \approx 1/N_a$. Consequently, the total air-path return reluctance can be summarized as follows:

$$\mathcal{R}_{air} = \mathcal{R}_{top} + \mathcal{R}_{body} + \mathcal{R}_{bottom} = \frac{1}{2\pi\mu_0 \cdot \sqrt{A}} + \frac{L}{\mu_0 \cdot 54A} + \frac{1}{2\pi\mu_0 \cdot \sqrt{A}} = \frac{1}{\mu_0}\left(\frac{L}{54A} + \frac{1}{\pi\sqrt{A}}\right) \tag{17}$$

The approximation $A_{eff} \approx 54A$ is specific to the aspect ratio (p = 5.06) of the core geometry considered in this study. For structures with substantially different aspect ratios, the demagnetizing factor N_a, and consequently this coefficient, must be re-derived from the formulation given by Joseph [24].

The leakage reluctance accounts for the leakage magnetic field that penetrates through the iron core between the coil and the moving plate, where h_{eff} represents the effective height of the leakage area. Significant leakage occurs between the top of the moving plate and the upper end of the iron core; therefore, the leakage reaches its maximum before the plate begins to move and its minimum when the plate is at its maximum height. In other words, h_{eff} is a dependent variable that varies with the plate position x, and the effective area decreases exponentially as x increases.

$$h_{\text{eff}} = h_{max} \cdot e^{-x/\lambda} \tag{18}$$

$$\mathcal{R}_{leak} = \frac{gap_{radial}}{\mu_0\left(2\pi r \cdot h_{eff}\right)} \tag{19}$$

In this context, λ is defined as the attenuation coefficient, which is set to the length of the iron core, and gap_{radial} represents the 1 mm clearance between the outer diameter of the core and the inner diameter of the moving plate. The total magnetic reluctance is expressed as $\mathcal{R}_{core} + \mathcal{R}_{air} + \mathcal{R}_{Leak}$ which serves as a dependent variable contingent on the displacement of the moving plate caused by the repulsive force.

This modeling was implemented using PSCAD simulation. By utilizing the duality principle, the system was configured with two electrical circuits (the main circuit and the eddy current circuit of the moving plate) and one magnetic circuit.

The physical design parameters of the iron core, the moving plate, and the superconducting element used throughout this study are summarized in Table 2. The coil turns and the quench resistance are treated as design variables and are varied according to the simulation scenarios.

Table 2. Physical Design Parameters of the Proposed SFCL-CB.

Component	Parameter	Value
Iron core	Length (L)	0.2 m
	Cross-sectional area (A)	0.0049 m^2 (49 cm^2)
	Relative permeability (μ_r)	5000
	Attenuation coefficient (λ)	0.2 m (set equal to core length)
Moving plate (MP)	Material	Aluminum
	Mass (m)	0.025 kg
	Eddy-current loop resistance	0.6 mΩ
	Outer/inner dimension (square)	80 mm/72 mm
	Cross-sectional area (A)	1.216×10^{-3} m^2 (annular, computed from the dimensions above)
	Radial gap to core (gap_{radial})	1 mm
	Initial position (x_0)	0.001 mm
	Maximum stroke	10 mm
Superconducting element	Material	$YBa_2Cu_3O_{-x}$ (YBCO) coated conductor
	Operating temperature	77 K (liquid-nitrogen bath)
	Critical current (I_C)	0.3 kA
	Quench resistance (R_{SC})	0.8–10 Ω (varied)
Driving coils	Number of turns (N_1, N_2)	Varied per scenario

2.3. Magnitude of Neglected Effects

The magnitude of the aerodynamic drag, guide friction, and non-ideal magnetic coupling neglected in Equation (12) is estimated below to quantify their influence on the mechanical separation time.

(a) Aerodynamic drag

Using the moving-plate dimensions in Table 2 (outer/inner square dimension 80 mm/72 mm, cross-sectional area A ≈ 1.216×10^{-3} m^2), a drag coefficient $C_d \approx 1.05$ for a bluff-body plate normal to the flow, and the plate velocity v (about 7.5 m/s for N_1 = 10t, rising to about 15 m/s for N_1 = 40t), the peak aerodynamic drag force $F_{drag} = 1/2 \cdot \rho_{air} \cdot C_d \cdot A \cdot v^2$ ranges from about 0.04 N to 0.18 N over these cases. Relative to the corresponding peak repulsion force (about 20 N to 100 N), this amounts to roughly 0.2% of the peak force, and a comparable contribution to the mechanical separation time.

(b) Guide friction

With the moving-plate mass m = 0.025 kg (Table 2) and a kinetic friction coefficient $\mu_k \approx 0.1$–0.2 typical for lubricated metal-on-metal contact, the peak frictional

force $F_{\text{friction}} = \mu_k \cdot m \cdot g$ is about 0.025–0.05 N, which is smaller than the peak repulsion force by roughly three orders of magnitude, corresponding to approximately 0.1–0.3% of the peak force and a similarly small contribution to the mechanical separation time.

(c) Non-ideal magnetic coupling

For windings sharing a common core, the coupling coefficient is typically k ≈ 0.99, decreasing toward k ≈ 0.97 for a comparatively looser winding arrangement. Since the mutual inductance M scales as k^2 (Equation (4)), and the induced imbalance voltage, eddy current, and peak repulsion force scale in turn with M and M^2 respectively, the peak force scales approximately as k^4. For k = 0.99 this corresponds to a reduction in peak force of about 3.9%, increasing to about 11.5% for k = 0.97. Using the design parameters in Table 2 (μ_r = 5000, N_1 = 10, N_2 = 80, S = 0.0049 m^2, l = 0.2 m), the mutual inductance M is calculated to be about eight times larger than L_1, confirming that the M-dependent term in Equation (2) dominates the induced imbalance voltage and supporting the k^4 scaling used above.

Combined, aerodynamic drag and guide friction together account for approximately 0.3–0.5% of the mechanical separation time, while the non-ideal coupling coefficient is the dominant of the three effects, contributing approximately 4–12% depending on the assumed value of k. Overall, the three effects are expected to account for approximately 4–12% of the mechanical separation time reported by the duality model, which represents a best-case value; a physical trial unit is expected to exhibit a moderately longer separation time within this margin.

3. Design of Simulation

3.1. Duality Modeling

Although PSCAD does not inherently support the implementation of magnetic coupling models or magnetic circuits such as iron cores, a coupled modeling approach between electrical and magnetic circuits is essential for accurate simulation. Since PSCAD lacks native support for magnetic circuit components, a feedback-based magnetic circuit model was developed by leveraging the mathematical duality between electrical and magnetic systems. The following Table 3 summarizes the conversion relationships between the magnetic and electric fields.

Table 3. Correspondence between Magnetic and Electric Circuit Parameters.

Description	Magnetic Domain	Electrical Domain
Driving Force	Magnetomotive Force (MMF, $\mathcal{F}$)	Voltage (V)
Field Intensity	Magnetic Field (H)	Electric Field (E)
Flow	Magnetic Flux (ϕ)	Electric Current (I)
Opposition	Reluctance ($\mathcal{R}$)	Resistance (R)
Ability	Permeance ($\mathcal{P}$)	Conductivity (G)
Energy	Magnetic Energy (W_m)	Electric Energy (W_e)

According to the Ampère-Maxwell equation, the curl of the magnetic field intensity is equal to the sum of the free current density and the partial derivative of the electric flux density with respect to time. When an electric current flows or an electric field varies, a magnetic field is induced in the surrounding space; in a coiled conductor, this magnetic field is generated in a direction that penetrates through the coil. The intensity of this magnetic field is proportional to the current flow, and the integration of this field intensity along a closed magnetic path yields the Magnetomotive Force (MMF).

In the simulation, a controlled voltage source and an ammeter are connected in series at the coil location of the electrical circuit, replacing the conventional inductor. The

Magnetomotive Force (MMF) is determined by the product of the number of turns and the current entering the winding; specifically, the MMF is calculated by multiplying the current I, measured by the ammeter, by the number of coil turns N. This calculated value serves as the driving force in the magnetic circuit and is implemented using a voltage source component within the simulation environment.

The following Figure 2 shows the mechanical structure and operational layout of the proposed SFCL-CB, in which the two coils N_1 and N_2 are wound on a common core, with the fixed plate (FP) mounted on top of the core and the moving plate (MP) placed directly above it. Magnetic flux is generated in the core by the currents through N_1 and N_2, and magnetic flux is also generated by the eddy-current circuit within the moving plate. The eddy currents induced in the plate produce a counter-magnetomotive force (counter-MMF) opposing the magnetic fields generated by the two coils. These coils and the moving plate interact through the magnetic coupling established by the shared core. Consequently, the moving plate experiences a magnetic repulsive force, leading to magnetic levitation.

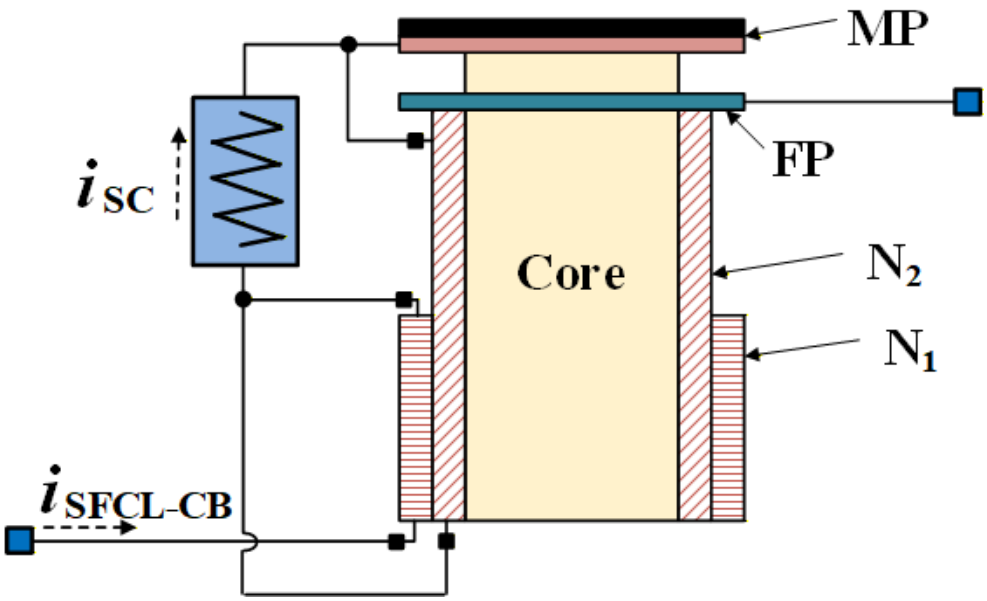


Figure 2. Mechanical Structure and Operational Layout of the Proposed SFCL-CB (Superconducting Fault Current Limiting Circuit Breaker) Components.

To account for this, an additional electrical circuit representing the eddy current of the moving plate must be constructed. The driving force of this internal circuit is induced according to Faraday's law, calculated as the product of the time derivative of the magnetic flux ($d\phi/dt$) and the number of turns (N), where N is assumed to be 1 for the moving plate. Furthermore, the internal electrical resistance of the moving plate can be indirectly derived using the resistivity of aluminum and the circumference of its outer diameter. To reflect the counter-MMF on the main circuit, the current flowing in the moving plate's internal circuit is implemented as a voltage source within the magnetic circuit.

The interconnection between the electrical and magnetic subcircuits in PSCAD/EMTDC is implemented as follows. In each physical winding branch of the electrical circuit, a controlled voltage source is placed in series with an ammeter; the source represents the back-EMF fed from the magnetic-circuit side and is set to $-N \cdot d\phi/dt$, where N is the number of turns and ϕ is the branch flux computed from the magnetic subcircuit. In the magnetic subcircuit, each reluctance is represented by a resistor, and each magnetomotive force (MMF) is represented by a controlled voltage source whose value is proportional to the product of the number of turns and the instantaneous winding current measured by the

electrical-side ammeter. Because N_1 and N_2 share the same core reluctance branches, their mutual coupling emerges naturally from the shared magnetic subcircuit without an explicit mutual-inductance element. The moving-plate eddy-current loop is modeled analogously, with an additional controlled voltage source of value $-d\phi/dt$ ($N = 1$ for a single-turn conducting ring) and the aluminum plate resistance derived from the resistivity and the ring perimeter. Figure 3a–c shows the three subcircuits and their controlled sources side by side.

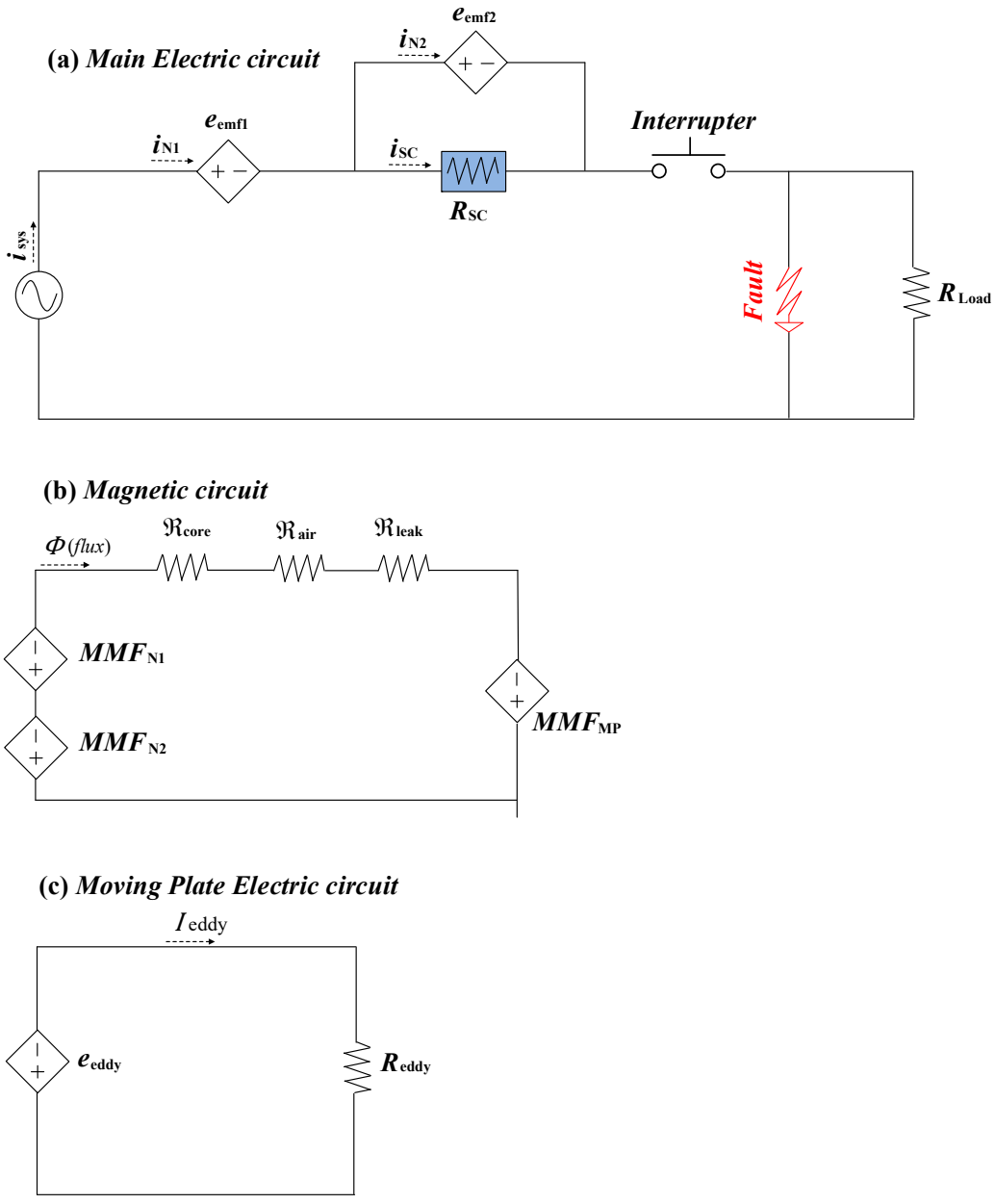


Figure 3. Proposed Duality-based SFCL-CB Modeling for the Electromagnetic Repulsion System (**a**) Main Electric Circuit (**b**) Magnetic Circuit (**c**) Moving Plate Electric Circuit.

When a magnetic material is present in the path of the magnetic field, the magnetic flux tends to flow through the material. The magnitude of this flux is determined by the material's relative permeability, cross-sectional area, and length. The ratio of the Magnetomotive Force (MMF) to the magnetic flux is defined as Reluctance ($\mathcal{R}$), which can vary depending on the specific sections along the magnetic path.

$$e_{emf} = -N\frac{d\phi}{dt},\ \phi = \frac{F}{R_m} = \frac{Ni}{R_m} \tag{20}$$

$$e_{emf} = -N\frac{d}{dt}\left(\frac{Ni}{R_m}\right) = \frac{N^2}{R_m}\frac{di}{dt} \tag{21}$$

3.2. Simulation Scenario

Instead of conducting hundreds of probabilistic simulations, this paper establishes deterministic worst-case scenarios with overlapping conditions of low SCR and system overloads to verify grid protection reliability. Under these environments, the enhanced protection reliability of the system is demonstrated by comparing conventional OCR-based protection with the proposed superconducting circuit breaker-based protection in terms of (1) the fault clearing speed and (2) the substantial reduction in blind zones.

Regarding the fault clearing speed characteristics of the SFCL-CB, the physical fault clearing behavior was investigated by varying the number of turns in N_1 and N_2, as well as the resistance of the superconducting element. The corresponding simulation scenarios are summarized in Table 4 below.

Table 4. Simulation Cases and Parameters for Characteristic of SFCL-CB (Superconducting Fault Current Limiting-Circuit Breaker).

Case No.	Variable	Value	Fixed Parameter
Case 1-1	Turns of N_1	10 [turns]	Turns of N_2: 80 [turns] Resistance of SC: 2 [Ω] SCR: 10
Case 1-2		20 [turns]	
Case 1-3		30 [turns]	
Case 1-4		40 [turns]	
Case 2-1	Turns of N_2	20 [turns]	Turns of N_1: 20 [turns] Resistance of SC: 2 [Ω] SCR: 10
Case 2-2		40 [turns]	
Case 2-3		60 [turns]	
Case 2-4		80 [turns]	
Case 3-1	Resistance of Superconductor	0.8 [Ω]	Turns of N_1: 30 [turns] Turns of N_2: 80 [turns] SCR: 10
Case 3-2		1.0 [Ω]	
Case 3-3		1.5 [Ω]	
Case 3-4		2.0 [Ω]	
Case 3-5		5.0 [Ω]	
Case 3-6		10.0 [Ω]	

To compare and analyze the performance with the conventional OCR while reflecting the breaking characteristics of the SFCL-CB, scenarios were established based on fault resistance and SCR. Under these scenarios, specific regions emerged where the conventional OCR either failed to trip or exhibited prolonged breaking times. In this paper, these regions are defined as blind zones. Table 5 below presents the scenario map designed to map the OCR blind zones according to the SCR and fault resistance.

Table 5. Scenario Map According to SCR and Fault Resistance.

R_{Fault} \ SCR	10^{-2} [Ω]	10^{-1} [Ω]	10^{0} [Ω]	10^{1} [Ω]	5×10^{1} [Ω]	10^{2} [Ω]
1	Case 4-1-1	Case 4-1-2	Case 4-1-3	Case 4-1-4	Case 4-1-5	Case 4-1-6
2	Case 4-2-1	Case 4-2-2	Case 4-2-3	Case 4-2-4	Case 4-2-5	Case 4-2-6
3	Case 4-3-1	Case 4-3-2	Case 4-3-3	Case 4-3-4	Case 4-3-5	Case 4-3-6
4	Case 4-4-1	Case 4-4-2	Case 4-4-3	Case 4-4-4	Case 4-4-5	Case 4-4-6

Table 5. *Cont.*

R_{Fault} \ SCR	10^{-2} [Ω]	10^{-1} [Ω]	10^{0} [Ω]	10^{1} [Ω]	5×10^{1} [Ω]	10^{2} [Ω]
5	Case 4-5-1	Case 4-5-2	Case 4-5-3	Case 4-5-4	Case 4-5-5	Case 4-5-6
6	Case 4-6-1	Case 4-6-2	Case 4-6-3	Case 4-6-4	Case 4-6-5	Case 4-6-6
7	Case 4-7-1	Case 4-7-2	Case 4-7-3	Case 4-7-4	Case 4-7-5	Case 4-7-6
8	Case 4-8-1	Case 4-8-2	Case 4-8-3	Case 4-8-4	Case 4-8-5	Case 4-8-6
9	Case 4-9-1	Case 4-9-2	Case 4-9-3	Case 4-9-4	Case 4-9-5	Case 4-9-6
10	Case 4-10-1	Case 4-10-2	Case 4-10-3	Case 4-10-4	Case 4-10-5	Case 4-10-6

To identify the blind zones of the OCR, the SCR of the simulation grid was varied. The grid source impedance for each SCR level was configured according to Equation (22), which defines the SCR. The grid source impedance was modeled using an R-$R//L$ structure, with the parallel damping factor (R_P/X_P ratio) set to 11. The calculations were performed by setting the line X/R ratio to 10, the rated power of the load ESS to 2.5 MW, and the nominal grid voltage to 13.22 kV_{rms}. The table below lists the grid source impedances corresponding to each SCR level.

$$SCR = \frac{S_{short\ \ circuit}}{P_n} \tag{22}$$

$$Z = \frac{V^2}{S_{short\ circuit}} \tag{23}$$

$$Z = R_s + \frac{R_p \cdot jX_p}{R_p + jX_p} \tag{24}$$

In Equation (22), the base power $S_{short\ circuit}$ is the short-circuit apparent power at the point of common coupling, and P_n is the rated apparent power of the connected inverter-based resource. For the scenarios considered in this paper, P_n = 2.5 MW at a nominal grid voltage of 13.22 kV_{rms}, so that the SCR values in Tables 5 and 6 (from 1 to 10) correspond to short-circuit capacities of 2.5 MVA to 25 MVA, as listed in Table 6.

Table 6. Calculated Equivalent Impedance of the Grid Power Source for Various SCRs.

SCR	$S_{short\ circuit}$ [MVA]	R_S (Series) [Ω]	R_P (Parallel) [Ω]	L_P (Parallel) [mH]	X_P (Parallel) [Ω]
1	2.5	0.6324	771.4883	186.04	70.1353
2	5	0.3162	385.7442	93.02	35.0677
3	7.5	0.2108	257.1628	62.01	23.3784
4	10	0.1581	192.8721	46.51	17.5338
5	12.5	0.1265	154.2977	37.21	14.0271
6	15	0.1054	128.5814	31.01	11.6892
7	17.5	0.0903	110.2126	26.58	10.0193
8	20	0.079	96.436	23.25	8.7669
9	22.5	0.0703	85.7209	20.67	7.7928
10	25	0.0632	77.1488	18.6	7.0135

4. Results and Discussion

Unlike a conventional overcurrent relay (OCR), the proposed superconducting fault current limiting circuit breaker (SFCL-CB) is an advanced protection device capable of fault current detection, current limiting, and interruption. Under normal operating conditions, the resistance of the superconducting element remains at zero, which makes the limiting coil current (i_{L1}) identical to the superconductor current (i_{SC}). Consequently, the magnetic flux inside the iron core is completely canceled out, maintaining a value of zero.

Figure 4 describes the transient voltage and current waveforms across each component of the SFCL-CB. Following the fault inception at 0.5 s, the relay initiates a trip signal within 1.5 ms (0.5015 s). The comparison among Cases 1-1 to 1-4 demonstrates a reduction in fault

clearing times, dropping from 0.647 s to 0.567 s, which implies that the current-limiting mechanism can be effectively accelerated through parametric optimization.

When a fault occurs at 0.5 s and the fault current surges, the trip actuation is initiated at 0.5015 s. At this instant, the magnetic flux balance within the iron core is disrupted, and the resulting magnetic flux induces an eddy current in the moving plate. This induced eddy current interacts with the actuation coil to generate an electromagnetic repulsion force that levitates the moving plate. As the moving plate rises, the magnitude of the leakage flux varies dynamically, maximizing the rate of change in magnetic energy. This accumulation of magnetic force pushes the total repulsion force to its peak magnitude. Furthermore, a larger number of turns (N_1) in Coil 1 enhances the magnetomotive force, thereby yielding a substantially higher peak force.

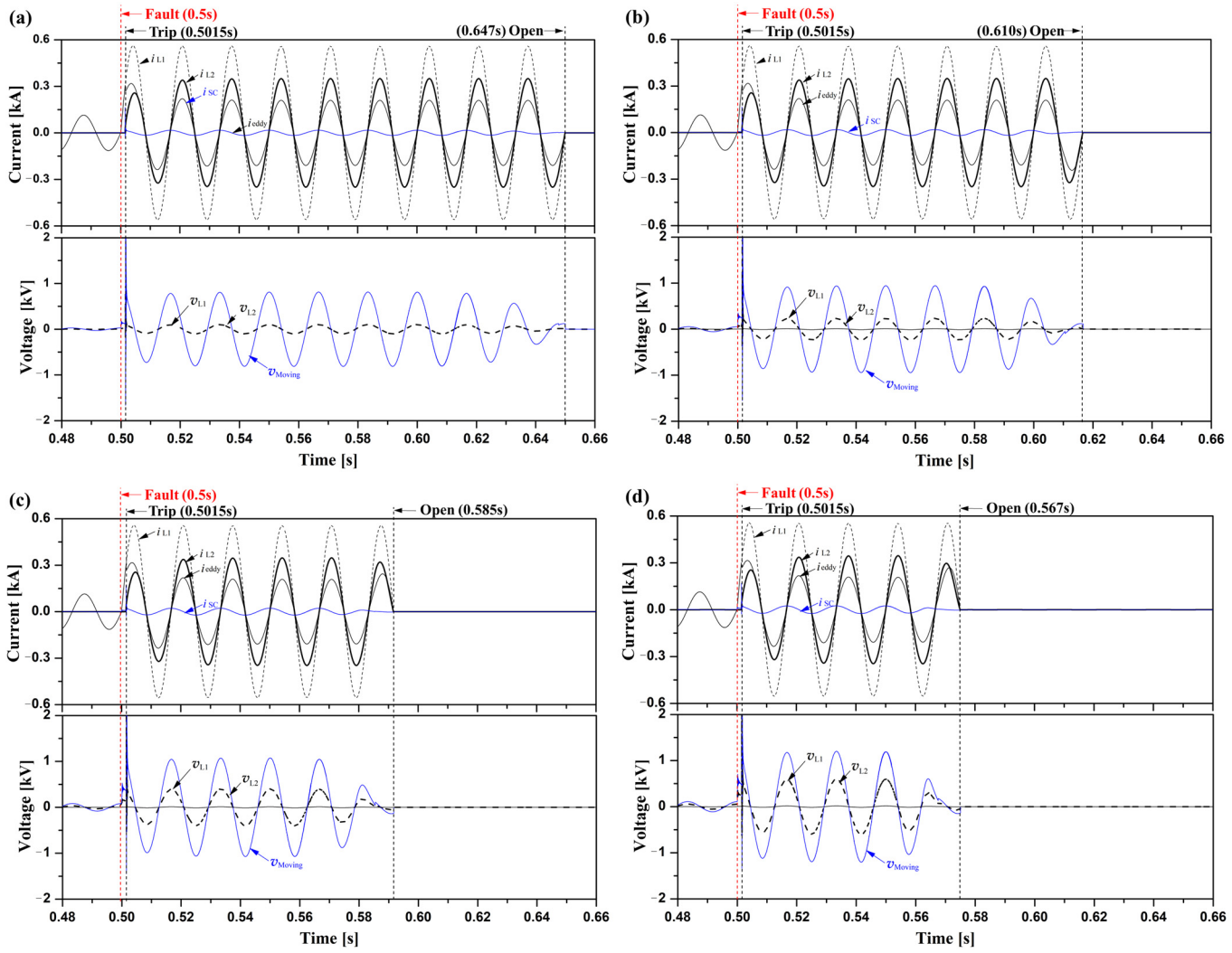


Figure 4. Coil 1&2 Current and Voltage Waveform, Eddy Current, Superconductor Current Waveform of Proposed SFCL-CB (Superconducting Fault Current Limiting Circuit Breaker) (**a**) Case 1-1 (**b**) Case 1-2 (**c**) Case-1-3 (**d**) Case 1-4.

Figure 5 presents the mechanical dynamic characteristics—comprising displacement (shift), velocity, and electromagnetic repulsion force—with respect to the number of turns in Coil 1(N_1). As N_1 increases from 10t (turns) to 40t, the initial electromagnetic repulsion force is generated much earlier with a higher peak magnitude. Consequently, the higher driving force boosts the opening velocity up to 16 m/s in the 40t condition, leading to the fastest mechanical separation at 0.567 s. These results verify that a larger number

of coil turns substantially enhances the protection sensitivity and operating speed of the proposed SFCL-CB.

Figures 6 and 7 describe the transient electrical waveforms and mechanical dynamic characteristics of the proposed SFCL-CB with respect to variations in the number of turns in Coil 2 (N_2). Following the fault inception at 0.5 s, the fault current surges, and the trip actuation is initiated at 0.5015 s via the protection relay. At this instant, the magnetic flux balance within the iron core is disrupted, and the resulting unbalanced magnetic flux induces a substantial eddy current (i_{eddy}) in the moving plate. This induced eddy current interacts with the driving coil(N_2) to generate an intensive electromagnetic repulsion force, which drives the levitation of the moving plate. Theoretically, the amplitude of the induced eddy current is proportional to the time rate of change of the magnetic flux (dB/dt), and the magnetic flux density (B) scales linearly with the number of coil turns (N_1 and N_2). Since the electromagnetic repulsion force exerted on the moving plate is proportional to the product of the eddy current density and the flux density ($F \propto B \cdot i_{eddy}$), the resultant repulsion force theoretically scales with the square of the turns in Coil 2. As the moving plate rises, the spatial distribution of the leakage flux varies dynamically, maximizing the rate of change in the stored magnetic energy. This accumulation of magnetic force pushes the total repulsion force to its peak magnitude, as shown in the bottom plot of Figure 7.

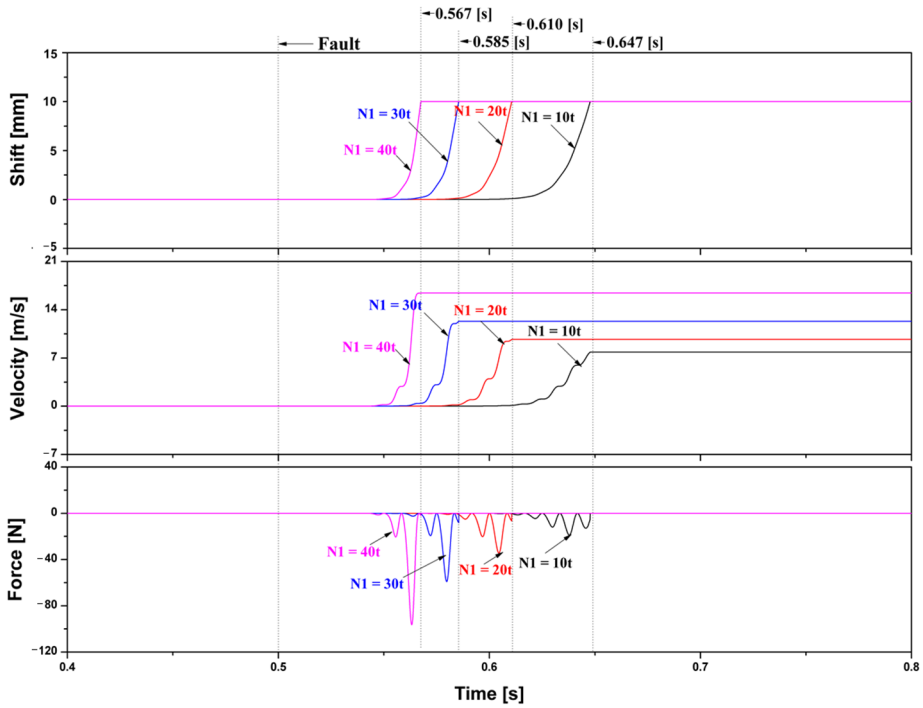


Figure 5. Dynamic characteristics of the breaker according to N_1 variations under fault conditions.

The increased value of N_2 prompts the fast displacement of the moving plate via the enhanced initial driving force, hence drastically widening the air gap between the driving coil and the plate within the nascent few milliseconds of operation. This spatial separation induces an immediate attenuation in both the mutual inductance and the time derivative of the magnetic flux ($d\phi/dt$), thereby inherently bounding the maximum magnitude of the induced eddy current. However, the total electromagnetic repulsion force ($F \propto B \cdot i_{eddy}$) still exhibits an exponential peak growth with higher N_2 values—as verified in Figure 7—owing to the predominant increase in the main flux density (B) dominating the eddy current stabilization. Accordingly, it can be confirmed from Figure 7 that a higher number of

turns in Coil 2 (N_2) substantially reinforces the mechanical driving force, subsequently accelerating the operating velocity of the moving contact.

The current commutation from the superconducting element to the coil 2 (N_2) is influenced by the magnitude of the quench resistance (R_{SC}). Based on the electric circuit model in Figure 3a, a higher R_{SC} increases the current diversion into the N_2 branch during the fault period. Inasmuch as the magnetomotive force (MMF) is a function of the coil current (i_{L2}), the increased current leads to changes in both the magnetic flux density (B) and the time derivative of the flux ($d\phi/dt$). Consequently, this electrical commutation induces an eddy current (i_{eddy}) change within the moving plate, subsequently increasing a repulsion force.

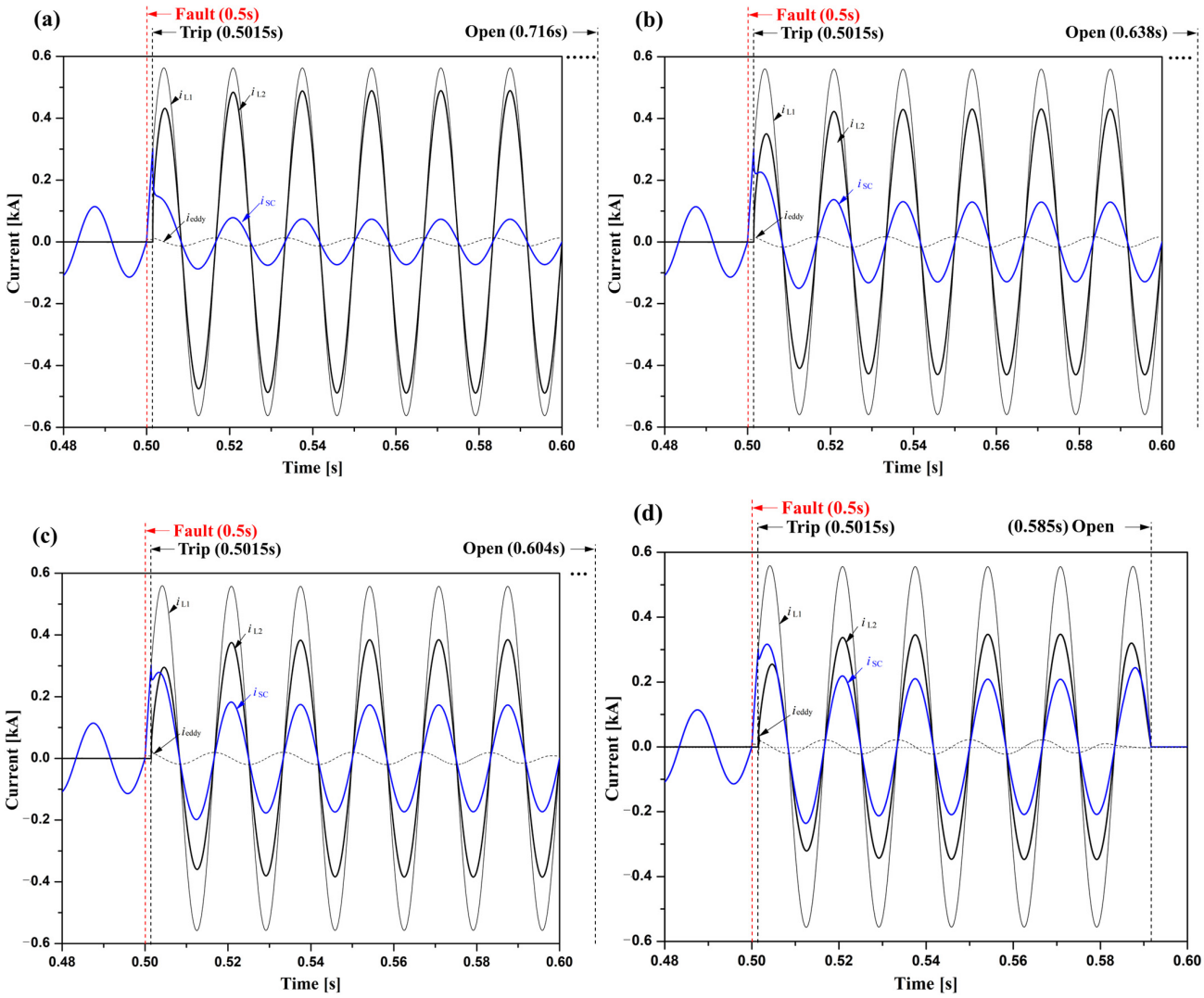


Figure 6. Coil 1&2 Current, Eddy Current, Superconductor Current Waveform of Proposed SFCL-CB (Superconducting Fault Current Limiting Circuit Breaker) (**a**) Case 2-1 (**b**) Case 2-2 (**c**) Case-2-3 (**d**) Case 2-4.

The increase in R_{SC} causes the fault current commutation into coil 2 (N_2), accelerating the fault interruption and simultaneously reducing the fault current through the superconducting element, which is advantageous for protecting the superconductor.

4.1. Sensitivity Analysis of Design Parameters

The influence of each design parameter on the mechanical response can be seen in the parametric sweep cases defined in Table 4 and the resulting mechanical response shown in

Figures 4–8. Increasing N_1 from 10 to 40 turns (Cases 1-1 to 1-4, Figures 4 and 5) reduces the mechanical separation time from 0.647 s to 0.567 s, an overall reduction of 12.4% over the fourfold change in turns. This reduction is not distributed evenly across the range: the separation time falls by 5.7% between 10 and 20 turns, by 4.1% between 20 and 30 turns, and by only 3.1% between 30 and 40 turns. Each additional increment of ten turns therefore yields a progressively smaller improvement, indicating a saturating rather than a linear relationship between N_1 and the mechanical response in this range.

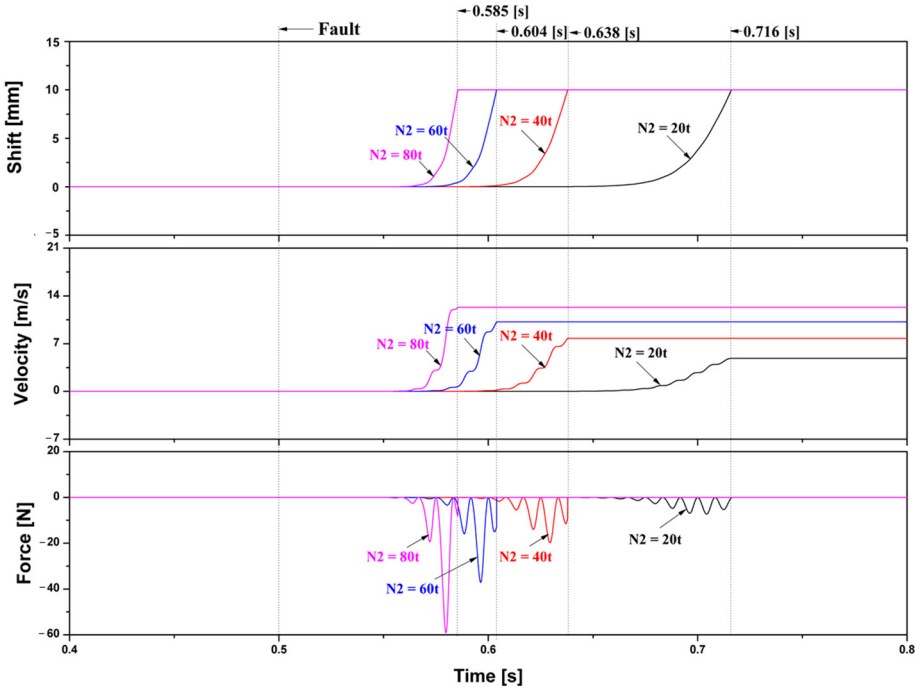


Figure 7. Dynamic characteristics of the SFCL-CB according to N_2 variations under fault conditions.

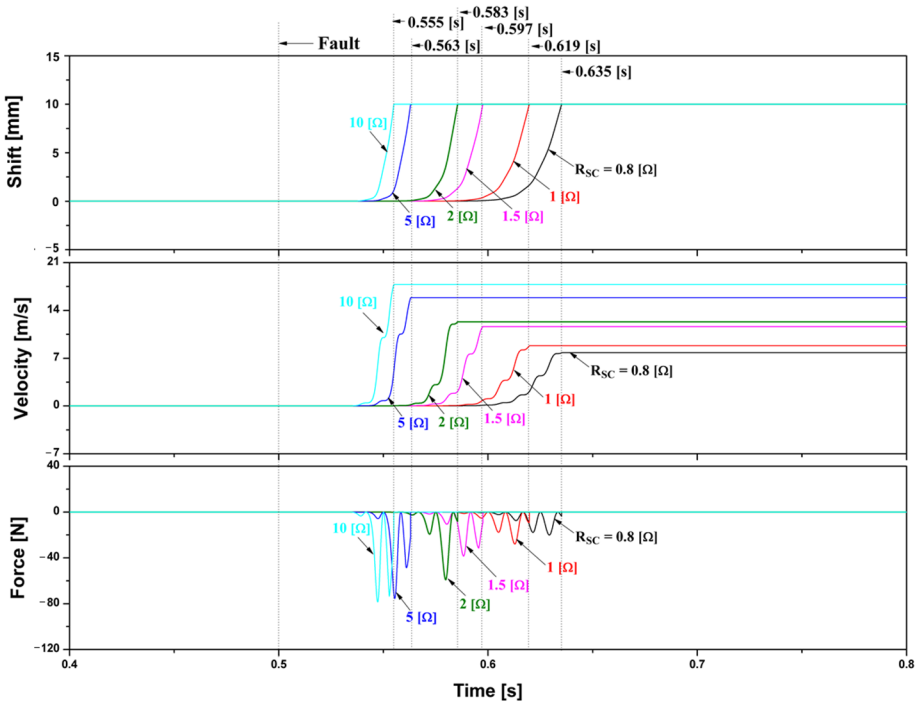


Figure 8. Dynamic characteristics of the SFCL-CB according to R_{SC} variations under fault conditions.

The N_2 sweep (Cases 2-1 to 2-4, Figures 6 and 7) follows the same saturating pattern but over a larger overall range. Increasing N_2 from 20 to 80 turns reduces the separation time from 0.716 s to 0.585 s, an overall reduction of 18.3%, with successive 20-turn increments producing reductions of 10.9%, 5.3%, and 3.1%. N_2 is therefore the more influential of the two winding parameters: a given proportional change in N_2 produces a larger change in separation time than the same proportional change in N_1. Expressed as a logarithmic sensitivity, that is the fractional change in separation time per fractional change in the parameter over the tested range, N_2 has a sensitivity of approximately -0.15 compared with approximately -0.10 for N_1.

The R_{SC} sweep (Cases 3-1 to 3-6, Figure 8) shows a comparatively small effect on separation time despite spanning a much wider relative range. Increasing R_{SC} from 0.8 Ω to 10 Ω, a twelvefold change, reduces the separation time from 0.635 s to 0.555 s, an overall reduction of 12.6%, with the individual steps (2.5%, 3.6%, 2.3%, 3.4%, and 1.4%, respectively) remaining consistently small rather than following a monotonic trend of their own. The resulting logarithmic sensitivity is approximately -0.05, roughly a third of the sensitivity to N_2, even though the R_{SC} sweep covers a substantially wider proportional range than either winding parameter.

This difference in sensitivity can be traced to how each parameter enters the force-generation mechanism. Under the same simplifying assumption used for N_2 in Section 2.2, namely that the winding current is approximately unchanged as the turns are varied, both N_1 and N_2 enter the driving force directly and to the second power: the flux density scales linearly with the number of turns, the eddy current follows dB/dt and therefore scales linearly with the turns as well, and since F is proportional to the product of the flux density and the eddy current, F scales as $(N)^2$ for either winding. N_2, however, has a second avenue of influence that N_1 does not share. Because $L_2 = \mu S(N_2)^2/L$, increasing N_2 also increases the branch inductance that sets the current time constant $\tau = L_2/R_{SC}$ governing how quickly current is established in the N_2 branch after the superconducting element quenches. N_2 therefore acts on the mechanical response through two channels at once, the $(N)^2$ amplitude term it shares with N_1 and the τ term that governs the timing of that force, which is why its logarithmic sensitivity is higher than N_1's even though both enter the force expression with the same power. R_{SC}, by contrast, does not appear in the force expression at all; it enters only through τ, so it governs how rapidly the current, and with it the force, develops after the fault rather than how large that force ultimately becomes. This is consistent with the comparatively weak effect of R_{SC} on separation time observed above: R_{SC} shifts the timing of a force whose magnitude it does not set, whereas N_1 and N_2 change the magnitude directly. Overall, the design tolerates moderate variation in all three parameters without a qualitative change in behavior, and N_2 is the parameter that most warrants tight control during manufacturing, since it is the only one of the three that acts through both channels.

4.2. Protection Blind Zone

Modern power systems are experiencing an increased integration of inverter-based resources (IBRs), such as photovoltaic systems, wind power plants, and energy storage systems (ESS), which subsequently reduces the short-circuit ratio (SCR). This decline in SCR decreases the fault current and amplifies the voltage drop, leading to failure to trip and false trip conditions in conventional protection systems. The proposed SFCL-CB features a characteristic where the generated force scales with the square of the current gradient. This attribute enables the distinction between fault currents and load fluctuations, allowing for a more sensitive response even to low fault currents.

To ensure a fair comparison, the OCR parameters used are summarized in Table 7. The settings reflect standard distribution-level practice for a feeder of the rated capacity considered in this paper.

Tables 8 and 9 present a comparative evaluation of the fault operation times and protection blind zones between the conventional OCR and the proposed SFCL-CB under varying short-circuit ratio (SCR) and fault resistance (R_{Fault}) conditions. As delineated in Table 8, the conventional OCR system exhibits a widespread blind zone (denoted by ×) and significant operation delays when the SCR decreases or R_{Fault} increases. In contrast, Table 9 shows that the proposed SFCL-CB restores operation across nearly the entire range of the examined conditions.

Table 7. Over Current Relay settings.

Parameter	Value Used in This Study
Pickup current, I_{pickup}	1.2 P.U.
Time-current characteristic	Standard inverse (IEC 60255-151) [26]
Time multiplier setting (TMS)	0.1

Table 8. Fault Clearing Time and Protection Blind Zone of Conventional OCR According to SCR and Fault Resistance.

R_{Fault} \ SCR	10^{-2} [Ω]	10^{-1} [Ω]	10^{0} [Ω]	10^{1} [Ω]	5×10^{1} [Ω]	10^{2} [Ω]
1	×	×	×	×	×	×
2	0.1572	0.1683	0.2691	0.4714	×	×
3	0.0445	0.0450	0.0603	0.1132	×	×
4	0.0270	0.0280	0.0325	0.0675	0.4989	×
5	0.0217	0.0220	0.0250	0.0495	0.3036	×
6	0.0168	0.0169	0.0197	0.0408	0.2621	×
7	0.0150	0.0151	0.0160	0.0362	0.2401	×
8	0.0140	0.0141	0.0155	0.0333	0.2257	×
9	0.0131	0.0132	0.0144	0.0313	0.2165	×
10	0.0125	0.0126	0.0136	0.0298	0.2100	×

Unit: [s]. OCR Warning Zone. OCR Blind Zone.

Table 9. Fault Clearing Time and Protection Blind Zone of proposed SFCL-CB According to SCR and Fault Resistance.

R_{Fault} \ SCR	10^{-2} [Ω]	10^{-1} [Ω]	10^{0} [Ω]	10^{1} [Ω]	5×10^{1} [Ω]	10^{2} [Ω]
1	0.1748	0.1748	0.1843	0.2051	×	×
2	0.0290	0.0285	0.0360	0.0556	0.0956	0.1314
3	0.0101	0.0102	0.0111	0.0273	0.0662	0.1000
4	0.0078	0.0079	0.0082	0.0178	0.0558	0.0889
5	0.0068	0.0068	0.0070	0.0149	0.04978	0.0829
6	0.0062	0.0062	0.0064	0.0132	0.0476	0.0802
7	0.0057	0.0057	0.0059	0.0100	0.0459	0.0779
8	0.0054	0.0054	0.0055	0.0088	0.0441	0.0762
9	0.0051	0.0051	0.0053	0.0082	0.0427	0.0751
10	0.0048	0.0048	0.0050	0.0077	0.0419	0.0744

Unit: [s]. Blue—OCR Warning Zone. Red—OCR Blind Zone. SFCL-CB Blind Zone.

The residual region where the SFCL-CB still fails to operate corresponds to very low SCR (=1) combined with high fault resistance ($R_{\text{Fault}} \geq 5 \times 10^1\ \Omega$), where the initial di/dt is insufficient to activate the electromagnetic repulsion mechanism. This region corresponds to the remaining $\times$ cells in Table 9.

Table 9 demonstrates the fault operation times and the recovery of protection blind zones achieved by integrating the proposed SFCL-CB under varying short-circuit ratio (SCR) and fault resistance (R_{Fault}) conditions. In contrast to the conventional OCR system, the SFCL-CB substantially reduces the OCR blind zones, that is the regions in which the conventional relay fails to trip, converting previous protection failures into reliable and rapid interruptions ranging from 0.029 s to 0.131 s even under high-fault-resistance and low-SCR environments. Furthermore, under highly robust grid conditions with an SCR of 10 and a bolted fault of $10^{-2}\ \Omega$, the device minimizes the fault clearing time down to 0.0048 s, verifying a substantial acceleration in the pure mechanical and electrical interruption velocity.

This comprehensive performance enhancement is entirely attributed to the unique driving mechanism of the SFCL-CB, which responds proportionally to the square of the current gradient rather than the absolute magnitude of the fault current. In weak power systems dominated by inverter-based resources (IBRs), the diminished fault current challenges the detection capability of standard inverse-time relays, but the steep initial surge slope of the fault remains identifiable. By sensitively capturing this current derivative, the SFCL-CB provides instantaneous electromagnetic repulsion force to drive the moving plate, thereby effectively suppressing severe voltage sags and completely blocking fault propagation toward the main grid.

5. Conclusions

In modern power systems with a high penetration of inverter-based resources (IBRs), the declining short-circuit ratio (SCR) drastically reduces fault current magnitudes, severely compromising the reliability of conventional protection schemes. To address these vulnerabilities, this paper presents an electromagnetic repulsion-based SFCL-CB designed for future distribution grids. By incorporating a superconducting element, the proposed device achieves zero power loss under normal operating conditions, and utilizes the rapid quench characteristic to initiate the subsequent current commutation process during a fault. Furthermore, through extensive parametric simulations evaluating various superconducting resistance values and winding numbers of N_1 and N_2 coils, the optimal design configuration was successfully established to maximize the electromagnetic repulsion force while stabilizing the overall commutation behavior.

While the declining short-circuit ratio (SCR) and high fault resistance under low-inertia conditions severely compromise the detection capability of conventional OCR-based protection schemes, the proposed technology provides a robust alternative through a dynamic force mechanism that scales with the square of the current gradient. Simulation results verify that the SFCL-CB substantially reduces the protection blind zones inherent to traditional relays, with a residual uncovered region only under very low SCR (=1) combined with very high fault resistance where the initial di/dt is insufficient to activate the repulsion mechanism, securing rapid and reliable load-side fault clearance within a maximum of 0.131 s even under highly degraded grid robustness. Ultimately, the ability of the proposed system to ensure swift mechanical isolation and effectively block fault propagation contributes to enhancing the protection reliability and operational stability of future distribution grids.

5.1. Practical Implementation Considerations

The SFCL-CB integrates the current-limiting and interrupting functions into a single device, reducing the number of separate protection components (relay, CT/PT, and conventional circuit breaker) relative to conventional schemes, at the cost of precision assembly of the coil–core–moving-plate mechanism. The flux-lock type SFCL structure and the electromagnetic-repulsion mechanical switch have been demonstrated in in-house trial units in [20,23], and extension to higher distribution voltage levels requires further insulation and cryogenic packaging design. The dominant cost component is the superconducting element together with its cryogenic cooling system, which is partially offset by the elimination of CT/PT and dedicated computational protection hardware. Maintenance of the superconducting element and the moving contact is comparable in effort to that of existing SFCL and vacuum or SF6 breaker installations. Because the device operates on a per-feeder basis, grid-wide deployment requires one SFCL-CB per protected feeder or section, in contrast to communication-based schemes that coordinate protection across multiple feeders from fewer installation points. Recovery of the YBCO element to the zero-resistance state after a quench is governed by the cryogenic system's capacity to remove the deposited heat; for liquid nitrogen-cooled YBCO SFCL elements at the current density considered here, recovery times are typically several seconds to tens of seconds, consistent with the previously reported trial units [21,23]. This recovery time sets the minimum reclose dead time for the SFCL-CB.

5.2. Limitations and Future Work

The validation reported in this paper is based on PSCAD/EMTDC duality-based simulation, and experimental verification has not yet been performed. The structural configuration of the SFCL-CB follows the flux-lock type SFCL and electromagnetic-repulsion mechanical switch trial units built and tested in-house in [18–23]; however, because the coil turns (N_1, N_2) and quench resistance identified as optimal in the present parametric study differ from those of the earlier units, a new trial unit reflecting this optimized design would need to be fabricated rather than reused directly. This study is intended as a design-optimization study, and fabricating this optimized trial unit and carrying out the corresponding experimental and hardware-in-the-loop (HIL) testing—incorporating source-impedance emulation, fault injection, and displacement and force sensing—are planned as future work.

Author Contributions: S.C.; writing—original draft, conceptualization, validation; S.-H.L.; writing—review and editing, formal analysis, supervision. All authors have read and agreed to the published version of the manuscript.

Funding: This research was funded by the Korea Institute of Energy Technology Evaluation and Planning (KETEP) grant funded by the Ministry of Climate, Energy and Environment. The Government of the Republic of Korea in 2025 (RS-2025-02317257).

Data Availability Statement: The original contributions presented in this study are included in the article. Further inquiries can be directed to the corresponding author.

Conflicts of Interest: Author Sangjae Choi was employed by the company Korea Electrical Safety Corporation. The remaining authors declare that the research was conducted in the absence of any commercial or financial relationships that could be construed as a potential conflict of interest.

Abbreviations

The following abbreviations are used in this manuscript:

SFCL-CB	Superconducting Fault Current Limiting-Circuit Breaker
ESS	Energy Storage System
IBR	Inverter-Based Resource
OCR	Over Current Relay
SCR	Short-Circuit Ratio
CT	Current Transformer
PT	Potential Transformer
MP	Moving Plate
MMF	Magnetomotive Force
SC	Superconducting

References

1. Kundur, P.; Paserba, J.; Ajjarapu, V.; Andersson, G.; Bose, A.; Cañizares, C.; Hatziargyriou, N.; Hill, D.; Stankovic, A.; Taylor, C.; et al. Definition and classification of power system stability IEEE/CIGRE joint task force on stability terms and definitions. *IEEE Trans. Power Syst.* **2004**, *19*, 1387–1401. [CrossRef]
2. Hatziargyriou, N.; Milanovic, J.; Rahmann, C.; Ajjarapu, V.; Canizares, C.; Erlich, I.; Hill, D.; Hiskens, I.; Kamwa, I.; Pal, B.; et al. Definition and Classification of Power System Stability—Revisited & Extended. *IEEE Trans. Power Syst.* **2021**, *36*, 3271–3281. [CrossRef]
3. Yang, Z.; Wang, H.; Liao, W.; Bak, C.L.; Chen, Z. Protection Challenges and Solutions for AC Systems with Renewable Energy Sources: A Review. *Prot. Control Mod. Power Syst.* **2025**, *10*, 18–39. [CrossRef]
4. Hamanah, W.M.; Hossain, M.I.; Shafiullah, M.; Abido, M.A. AC Microgrid Protection Schemes: A Comprehensive Review. *IEEE Access* **2023**, *11*, 76842–76868. [CrossRef]
5. *IEEE C37.100-1992*; IEEE Standard Definitions for Power Switchgear. IEEE: New York, NY, USA, 1992.
6. Sharaf, H.M.; Zeineldin, H.H.; Ibrahim, D.K.; El Zahab, E.E.D.A. Protection coordination of directional overcurrent relays considering fault current direction. In *Proceedings of the 2014 IEEE PES Innovative Smart Grid Technologies Conference Europe (ISGT-Europe), Istanbul, Turkey, 12–15 October 2014*; IEEE: New York, NY, USA, 2014; pp. 1–5.
7. Farkhani, J.S.; Zareein, M.; Soroushmehr, H.; Mortazavi, H.M. Coordination of Directional Overcurrent Protection Relay for Distribution Network with Embedded DG. In *Proceedings of the 2019 5th Conference on Knowledge Based Engineering and Innovation (KBEI), Tehran, Iran, 28 February–1 March 2019*; IEEE: New York, NY, USA, 2019; pp. 281–286.
8. Ukil, A.; Deck, B.; Shah, V.H. Smart distribution protection using current-only directional overcurrent relay. In *Proceedings of the 2010 IEEE PES Innovative Smart Grid Technologies Conference Europe (ISGT Europe), Gothenburg, Sweden, 11–13 October 2010*; IEEE: New York, NY, USA, 2010; pp. 1–7.
9. Lim, S.-H.; Lim, S.-T. Analysis on Coordination of Over-Current Relay Using Voltage Component in a Power Distribution System with a SFCL. *IEEE Trans. Appl. Supercond.* **2019**, *29*, 5603605. [CrossRef]
10. Eladl, A.A.; Sheta, A.N.; Elgamal, M.; Vasquez, J.C.; Sedhom, B.E. Optimal directional overcurrent relay settings for stable microgrids with synchronous and inverter-based resources. *Int. J. Electr. Power Energy Syst.* **2025**, *167*, 110639. [CrossRef]
11. Dash, S.; Jena, M.K.; Achlerkar, P.D.; Shaw, P. Exploring the interdependence between control and protection philosophies in inverter integrated power system: A case study on directional relaying schemes. *Electr. Power Syst. Res.* **2024**, *228*, 110074. [CrossRef]
12. Ataee-Kachoee, A.; Hashemi-Dezaki, H.; Ketabi, A. Optimized adaptive protection coordination of microgrids by dual-setting directional overcurrent relays considering different topologies based on limited independent relays' setting groups. *Electr. Power Syst. Res.* **2023**, *214*, 108879. [CrossRef]
13. Quispe, J.C.; Orduña, E. Transmission line protection challenges influenced by inverter-based resources: A review. *Prot. Control Mod. Power Syst.* **2022**, *7*, 28. [CrossRef]
14. Aftab, M.A.; Hussain, S.M.S.; Ali, I.; Ustun, T.S. Dynamic protection of power systems with high penetration of renewables: A review of the traveling wave based fault location techniques. *Int. J. Electr. Power Energy Syst.* **2020**, *114*, 105410. [CrossRef]
15. Wilches-Bernal, F.; Bidram, A.; Reno, M.J.; Hernandez-Alvidrez, J.; Barba, P.; Reimer, B.; Montoya, R.; Carr, C.; Lavrova, O. A survey of traveling wave protection schemes in electric power systems. *IEEE Access* **2021**, *9*, 72949–72969. [CrossRef]
16. Gutierrez-Rojas, D.; Nardelli, P.H.J.; Mendes, G.; Popovski, P. Review of the State-of-the-Art on Adaptive Protection for Microgrids based on Communications. *arXiv* **2020**, arXiv:2007.13479.
17. *IEC 61850-1*; Communication Networks and Systems for Power Utility Automation—Part 1: Introduction and Overview. International Electrotechnical Commission: Geneva, Switzerland, 2013.

18. Lim, S.-H.; Choi, H.-S.; Han, B.-S. Fault current limiting characteristics due to winding direction between coil 1 and coil 2 in a flux-lock type SFCL. *Phys. C Supercond.* **2004**, *416*, 34–42. [CrossRef]
19. Lim, S.-H.; Han, T.-H.; Choi, H.-S.; Han, B.-S.; Lee, S.-W. Quench characteristics of HTSC elements in integrated three-phase flux-lock type SFCL according to ground-fault types. *Phys. C Supercond. Its Appl.* **2007**, *463*, 1198–1203. [CrossRef]
20. Park, M.-K.; Choi, S.-J.; Lim, S.-H. Current Limiting and Interrupting Operations of Flux-Lock Type SFCLI Using Mechanical Switch. *IEEE Trans. Appl. Supercond.* **2020**, *30*, 5601805. [CrossRef]
21. Lim, S.-H.; Kim, J.-C.; Lee, B.-W. Improvement of Recovery Characteristics of a Flux-Lock Type SFCL Using a Superconductor's Trigger. *IEEE Trans. Appl. Supercond.* **2010**, *20*, 1182–1185. [CrossRef]
22. Lim, S.-H. Operational Characteristics of Flux-Lock Type SFCL with Series Connection of Two Coils. *IEEE Trans. Appl. Supercond.* **2007**, *17*, 1895–1898. [CrossRef]
23. Lim, S.-H.; Ahn, H.-J.; Park, C. Study on Fault Current Limiting Characteristics of an SFCL Using Magnetic Coupling of Two Coils with Mechanical Switch Driven by Electromagnetic Repulsion Force. *IEEE Trans. Appl. Supercond.* **2014**, *24*, 5600704. [CrossRef]
24. Joseph, R.I. Ballistic Demagnetizing Factor in Uniformly Magnetized Cylinders. *J. Appl. Phys.* **1966**, *37*, 4639–4643. [CrossRef]
25. Noe, M.; Steurer, M. High-temperature superconductor fault current limiters: Concepts, applications, and development status. *Supercond. Sci. Technol.* **2007**, *20*, R15–R29. [CrossRef]
26. *IEC 60255-151*; Measuring Relays and Protection Equipment—Part 151: Functional Requirements for Over/Under Current Protection. International Electrotechnical Commission: Geneva, Switzerland, 2009.

Disclaimer/Publisher's Note: The statements, opinions and data contained in all publications are solely those of the individual author(s) and contributor(s) and not of MDPI and/or the editor(s). MDPI and/or the editor(s) disclaim responsibility for any injury to people or property resulting from any ideas, methods, instructions or products referred to in the content.